

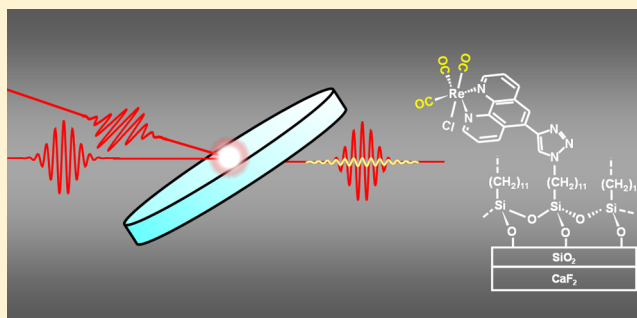
# Orientalional Dynamics of a Functionalized Alkyl Planar Monolayer Probed by Polarization-Selective Angle-Resolved Infrared Pump–Probe Spectroscopy

Jun Nishida, Chang Yan, and Michael D. Fayer\*

Department of Chemistry, Stanford University, Stanford, California 94305, United States

**S** Supporting Information

**ABSTRACT:** Polarization-selective angle-resolved infrared pump–probe spectroscopy was developed and used to study the orientational dynamics of a planar alkylsiloxane monolayer functionalized with a rhenium metal carbonyl headgroup on a SiO<sub>2</sub> surface. The technique, together with a time-averaged infrared linear dichroism measurement, characterized picosecond orientational relaxation of the headgroup occurring at the monolayer–air interface by employing several sets of incident angles of the infrared pulses relative to the sample surface. By application of this method and using a recently developed theory, it was possible to extract both the out-of-plane and “mainly”-in-plane orientational correlation functions in a model-independent manner. The observed correlation functions were compared with theoretically derived correlation functions based on several dynamical models. The out-of-plane correlation function reveals the highly restricted out-of-plane motions of the head groups and also suggests that the angular distribution of the transition dipole moments is bimodal. The mainly-in-plane correlation function, for the sample studied here with the strongly restricted out-of-plane motions, essentially arises from the purely in-plane dynamics. In contrast to the out-of-plane dynamics, significant in-plane motions occurring over various time scales were observed including an inertial motion, a restricted wobbling motion of  $\sim 3$  ps, and complete randomization occurring in  $\sim 25$  ps.



## 1. INTRODUCTION

Molecules bound at interfaces are expected to exhibit fundamentally different structures and dynamics compared with those in bulk solutions. Because of the very existence of interfaces, environments surrounding interfacial molecules are no longer isotropic. Such anisotropic structures and dynamics play important roles in the unique properties of interfacial molecules such as enhanced reactivity and enantioselectivity in some heterogeneous catalysts.<sup>1,2</sup> Therefore, characterization of interfacial molecular structures and their time evolution is of central importance in understanding the properties and applications of functionalized surface monolayers. While the time-averaged nature of interfacial molecular structures has been intensively studied by numerous techniques such as sum frequency generation (SFG) spectroscopy,<sup>3–5</sup> motions of interfacial molecules, particularly in the ultrafast regime, have not been fully understood. Such dynamical motions of interfacial molecules can be most directly probed by observing orientational relaxations of molecules through polarization-selective spectroscopic methods. In these methods, molecules are pumped with a certain polarization and then, after time  $t$ , probed with a polarization either parallel ( $\parallel$ ) or perpendicular ( $\perp$ ) to the pump polarization, yielding time-dependent signals  $R_{\parallel}(t)$  and  $R_{\perp}(t)$ , respectively.

Many polarization-selective experiments used to understand molecular orientational dynamics at liquid–air/solid–air interfaces have been developed including fluorescence depolarization for nanosecond (ns) dynamics,<sup>6–8</sup> time-resolved sum-harmonic generation (TRSHG) experiments for subnanosecond (sub-ns) dynamics,<sup>9</sup> and, most recently, time-resolved vibrational sum-frequency generation (TRVSG) experiment for picosecond (ps) dynamics.<sup>10</sup> In some remarkable fluorescence/SHG experiments to study  $>$ sub-ns dynamics, beam geometries and polarizations have been configured such that in-plane and out-of-plane dynamics of molecules can be addressed separately.<sup>6–9</sup> In these studies, it was necessary to assume the decoupling of the in-plane and out-of-plane motions of molecules to interpret the observed signals. Distinct in-plane and out-of-plane motions were observed for the relatively slow motions. However, the extraction of in-plane and out-of-plane motions has not been possible in the ultrafast regime because of the lack of an experimental technique and the theoretical framework to characterize ultrafast molecular dynamics in anisotropic systems including planar interfaces.

Infrared (IR) polarization-selective pump–probe spectroscopy has been successful in providing detailed dynamical pictures of picosecond molecular reorientation in isotropic media, such as

Received: August 18, 2016

Published: September 26, 2016

bulk water.<sup>11–13</sup> It is desirable to extend IR pump–probe spectroscopy to the study of reorientation dynamics of molecules at planar surfaces. Recently, a methodology was theoretically formulated to extract two orientational correlation functions, corresponding to out-of-plane and “mainly”-in-plane motions, in a model-independent and assumption-free manner.<sup>14</sup> The key is that anisotropy measurements must be made with at least two incident angles of the pump/probe beams relative to the surface normal. The time-dependent measurements are then combined with the results from time-averaged infrared linear dichroism (IRLD) measurements. Here we experimentally demonstrated the application of IR polarization-selective angle-resolved pump–probe (PSAR–PP) spectroscopy on an alkyl chain (C<sub>11</sub>) monolayer functionalized with metal carbonyl head groups that serve as the vibrational probes. The previous theory was extended to include detailed consideration of wobbling-in-a-cone dynamics. The local field corrections for the pump–probe geometry were derived and applied. The results elucidate the detailed picosecond motions of the headgroup/alkyl chains on the interface. The combination of theory and experiment yielded a comprehensive description of the out-of-plane and in-plane orientational dynamics.

## 2. RESULTS AND DISCUSSION

**2.1. Monolayer Sample and Time-Averaged Infrared Linear Dichroism.** Figure 1A shows the structure of the functionalized alkylsiloxane monolayer. The rhenium metal

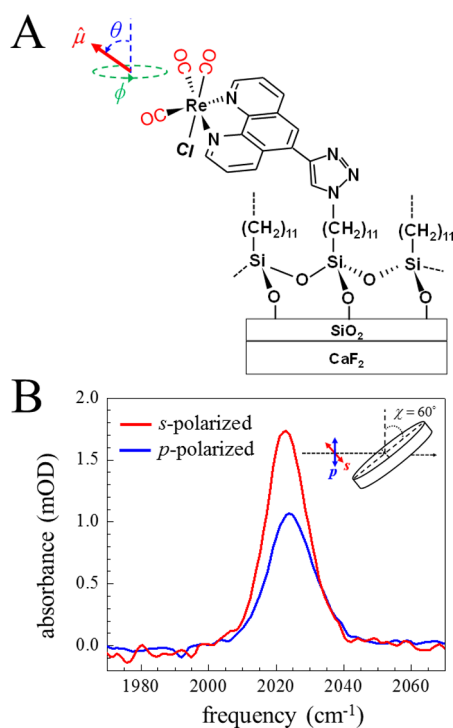


**Figure 1.** (A) Schematic illustration of the structure of the C<sub>11</sub> alkylsiloxane monolayer functionalized with the rhenium metal carbonyl group.  $\hat{\mu}$  is a unit vector parallel to the transition dipole moment of the CO symmetric stretch mode. The polar angle of  $\hat{\mu}$  with respect to the surface normal is denoted as  $\theta$ , while the azimuthal angle is written as  $\phi$ . (B) IR absorption linear dichroism observed at the incident angle  $\chi = 60^\circ$ . The *s*-polarized beam is more strongly absorbed than the *p*-polarized beam ( $A_p/A_s = 0.62$  at  $2023.5 \pm 5 \text{ cm}^{-1}$ ), which demonstrates that the polar orientations of the head groups and thus the transition dipoles are ordered relative to the surface.

carbonyl head groups, which serve as vibrational chromophores, are tethered to the SiO<sub>2</sub> network by the C<sub>11</sub> alkyl chains. This functionalized monolayer has been extensively studied by two-dimensional IR spectroscopy to elucidate the broadening mechanism of the IR absorption band, and the time dependence of the spectral diffusion, which provides information on the structural evolution of the headgroup/alkyl chain system.<sup>15–18</sup> The results revealed that the band is substantially inhomogeneously broadened, and spectral diffusion occurs with a time constant of  $\sim 35$  ps.<sup>17</sup> This  $\sim 35$  ps spectral diffusion is caused by the complex interplay between the fluctuation of the surrounding monolayer structure and the headgroup motion itself.<sup>19</sup> In contrast, PSAR–PP spectroscopy specifically characterizes the orientational motions of the headgroup with its attached alkyl chain.

A thin layer of SiO<sub>2</sub> was deposited on an IR transmitting CaF<sub>2</sub> substrate. The thicknesses of the SiO<sub>2</sub> and CaF<sub>2</sub> layers are  $\sim 100$  nm and  $\sim 3$  mm, respectively. The SiO<sub>2</sub>/CaF<sub>2</sub> substrate is almost perfectly transparent for  $>1000 \text{ cm}^{-1}$  IR beams. The CO symmetric stretching mode of the headgroup was used as the vibrational probe. The transition dipole moment for this mode points toward the line that connects the rhenium atom and the center of gravity for the three carbonyls. The directional motion of this transition dipole is monitored in the following experiments. The transition dipole’s polar angle relative to the surface normal is denoted as  $\theta$ , while the azimuthal angle is denoted as  $\phi$ .

To obtain the average direction of the transition dipoles on the surface, time-averaged infrared absorption linear dichroism (IRLD) was recorded using a Fourier transform infrared (FT-IR) spectrometer. Figure 1B shows the IR absorption spectra of the CO symmetric stretching mode for *s*- (red) and *p*- (blue) polarized incident beams with the incident angle  $\chi = 60^\circ$ . The absorption cross-section is polarization-dependent, which demonstrates that the head groups’ polar orientations are ordered on the surface.

**2.2. Deriving Order Parameter: Local Field Correction.** On the basis of the IR linear dichroism shown in Figure 1B, the average polar orientation of the headgroup on the surface can be deduced. We are interested in the order parameter  $\langle S \rangle \equiv \langle (3 \cos^2 \theta - 1)/2 \rangle$ , where  $\langle \dots \rangle$  denotes the ensemble average over all the molecules in the beam focus. It should be noted that the *E*-field right at the air–substrate interface is different from the field in the air; this difference is often neglected in this type of experiment. The procedure to convert a field in bulk media (air/substrate) to a field at an interface is often referred to as the “local field correction” and was developed in the context of SFG spectroscopy.<sup>3–5,20</sup> In the Supporting Information, we discuss the local field correction for IRLD experiment using a three-layer model (Figure S1; eq S.12). The local field correction scheme can be extended to PSAR–PP spectroscopy as discussed further (Figure S2; eq S.22). It is shown that, after the local field correction is taken into account, the observed dichroic ratio in Figure 1B is related to the order parameter  $\langle S \rangle \equiv \langle (3 \cos^2 \theta - 1)/2 \rangle$  by

$$\rho(\chi) \equiv \frac{A_p(\chi)}{A_s(\chi)} = a_{p/s} \left( 1 + 3 \sin^2 \chi' \frac{\langle S \rangle}{1 - \langle S \rangle} \right) \quad (1)$$

where  $A_p(\chi)$  and  $A_s(\chi)$  are the absorption cross-sections for *p*- and *s*-polarized beams with the incident angle  $\chi$ . The *p*/*s* enhancement factor  $a_{p/s}$  and the effective incident angle  $\chi'$  arise from the local field correction and are both dependent on the

incident angle  $\chi$  (eq S.10). For  $\chi = 60^\circ$ ,  $a_{p/s} = 1.011$  and  $\chi' = 49.72^\circ$ . From eq 1 and the measured dichroic ratio, the order parameter  $\langle S \rangle$  can be determined.

We performed IRLD experiment for series of incident angles from  $0^\circ$  to  $60^\circ$ . The order parameter was found to be  $\langle S \rangle = -0.290 \pm 0.016$  (Figure S3). The order parameter obtained here is important for interpreting the following dynamical measurements with PSAR–PP spectroscopy.

**2.3. PSAR–PP Implementation.** The polarization configuration used in PSAR–PP experiment is shown in Figure 2, and more concise conceptual representations can be found in Figure 3A and Figure 3B insets. PSAR–PP spectroscopy is essentially a time-resolved linear dichroism measurement. In PSAR–PP spectroscopy, the polarization-selective measurements were implemented in two geometries. In both geometries, the pump beam is always set to be *s*-polarized, and the probe beam's polarization is set either parallel or perpendicular to the pump polarization. In the first “normal” geometry, the sample wafer was placed normal to the probe beam's propagation direction as in Figure 3A inset. Thus, both parallel and perpendicular polarizations of the probe beam are *s*-polarized. The signals observed in this “normal” geometry are  $R_{\parallel}^{\chi=0^\circ}(t)$  and  $R_{\perp}^{\chi=0^\circ}(t)$ , respectively. In the second “tilted” geometry, the wafer is placed such that the probe beam's incident angle to the surface is  $\chi = 60^\circ$  as in Figure 3B inset. As a result, the parallel polarization for the probe is *s*-polarized, while the perpendicular polarization is *p*-polarized. The signals in the “tilted” geometry are  $R_{\parallel}^{\chi=60^\circ}(t)$  and  $R_{\perp}^{\chi=60^\circ}(t)$ .

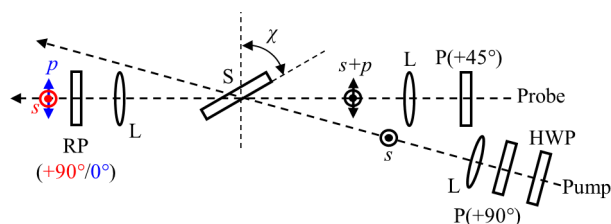


**Figure 2.** Beam and polarization geometry for the PSAR–PP experiment. The pump beam's polarization is rotated by a half-wave plate (HWP) and cleaned up by a fixed polarizer (P) to be *s*-polarized ( $+90^\circ$ ). The pump beam is focused by a  $f = 15$  cm lens (L) into the sample (S). The probe beam's polarization is set to be  $+45^\circ$ , which contains both *s*- and *p*- polarizations, and focused by a  $f = 10$  cm lens into the sample. The incident angle of the probe into the sample surface is the tilt angle  $\chi$ . The transmitted probe beam is collimated by a lens, and the polarization is resolved by a resolving polarizer (RP) on a motorized rotation stage. The polarization of the resolving polarizer is set to be  $+90^\circ$  (*s*-polarized) when a “parallel” signal is recorded and  $0^\circ$  (*p*-polarized for  $\chi \neq 0^\circ$ ) when a “perpendicular” signal is recorded. Note that to extract the orientational correlation functions, PSAR–PP spectroscopy must be implemented in two geometries. In the “normal” geometry (Figure 3A), the tilt angle  $\chi$  was set to  $0^\circ$ , while in the “tilted” geometry (Figure 3B),  $\chi$  was set to  $60^\circ$ .

As shown in Figure 2, in the actual setup, the pump polarization was set to  $90^\circ$  (vertical relative to the optical table), and the probe polarization was set to  $45^\circ$  before the sample. After the probe beam passed through the sample and the substrate, the polarization was resolved to either  $90^\circ$  (parallel) or  $0^\circ$  (perpendicular) with a polarizer on a computer controlled rotation stage to record the parallel and perpendicular signals, respectively. Then the probe was projected back to  $45^\circ$  by passing through a final polarizer, frequency-dispersed by a

spectrograph, and detected by a 32-elements MCT detector. The signal was recorded as

$$\frac{I_{\text{on}} - I_{\text{off}}}{I_{\text{off}}} \quad (2)$$

where  $I_{\text{on}}$  is the probe beam intensity with the pump on, while  $I_{\text{off}}$  is that with no pump. This polarization and beam configuration guarantees that the parallel and perpendicular signals are obtained with identical geometries and parallel/perpendicular signal amplitudes are absolutely comparable. It is also advantageous that the generated third-order signal is self-heterodyned by the probe pulse as a local oscillator, and the probe and the signal pass through exactly the same path and experience exactly the same number of reflections at surfaces. Therefore, any effects that alter the amplitude of the third-order signal in and after the sample can be accounted for by dividing the heterodyned signal ( $I_{\text{on}} - I_{\text{off}}$ ) by the local oscillator intensity ( $I_{\text{off}}$ ) as in eq 2. Another important feature of the setup is that the observed signals are insensitive to the crossing angle between the pump and probe beams; as seen in Figure 2, the pump polarization is in the plane of the surface regardless of the crossing angle, and thus the crossing angle does not have to be taken into account.<sup>14</sup> These features significantly facilitate the interpretation of the observed signals.

The pump beam is the output from Germanium acousto-optic modulator pulse shaping system, and the phase of the pump pulse was cycled during the measurements to remove interference caused by a minor amount of scattered light from the surface.<sup>21</sup> Also, the lower frequency component ( $<1950$   $\text{cm}^{-1}$ ) of the pump pulse was filtered by the pulse shaping system such that the antisymmetric modes of the headgroup located around  $\sim 1900$   $\text{cm}^{-1}$  are not pumped.<sup>22,23</sup>

The strong optical transition of the CO symmetric stretching mode can be saturated when the pump power is relatively high, and the extent of the saturation is different for parallel and perpendicular signals. This difference causes the parallel and perpendicular signals to have the incorrect relative amplitudes for use in the determination of the anisotropy. Therefore, the pump pulse intensity was attenuated so that the measurements were free of saturation (Figure S4). Further details can be found in the Supporting Information.

**2.4. PSAR–PP Results and Extraction of the Correlation Functions.** The signals obtained in each of the two geometries are shown in Figure 3A and Figure 3B. Although the signals arising from a single layer of molecules are very small, they are clean enough to discern a few qualitative features. As seen in Figure 3A, the two signals in the “normal” geometry,  $R_{\parallel}^{\chi=0^\circ}$  and  $R_{\perp}^{\chi=0^\circ}$ , are initially significantly different in their amplitudes, but as  $t$  becomes large, the difference in the amplitudes is reduced and then vanishes. Because all the pump/probe polarizations are in-plane in the “normal” geometry, this reduction in the amplitude difference should be attributed to a significant in-plane orientational motion of the transition dipole. In Figure 3B,  $R_{\perp}^{\chi=60^\circ}(t)$  is much smaller in amplitude than  $R_{\parallel}^{\chi=60^\circ}(t)$ . This observation is consistent with the result of time-averaged linear dichroism measurement that *p*-polarization interacts less with the transition dipoles than *s*-polarization (Figure 1B). It can also be seen that  $R_{\perp}^{\chi=0^\circ}(t)$  in Figure 3A and  $R_{\perp}^{\chi=60^\circ}(t)$  in Figure 3B are slightly different in their temporal profiles because the influences of in-plane motions and out-of-plane motions on the signals are different.

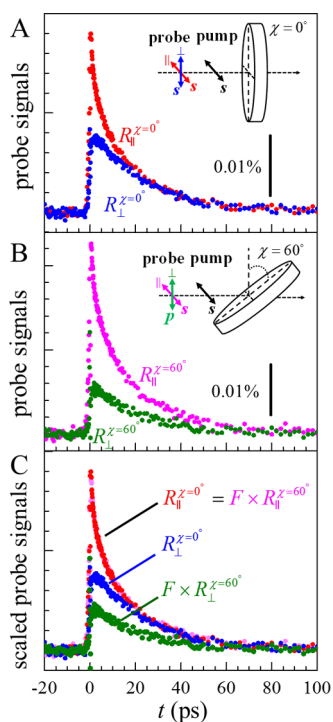


**Figure 3.** (A) Pump–probe signals at  $2023.5\text{ cm}^{-1}$  acquired in the “normal” geometry as shown in the inset. Note that in this geometry, all the polarizations involved are  $s$ -polarized. The parallel signal  $R_{||}^{\chi=0^\circ}$  is obtained by setting the probe polarization parallel to the pump polarization, while the perpendicular signal  $R_{\perp}^{\chi=0^\circ}$  is acquired by setting the probe polarization perpendicular to the pump polarization. (B) Pump–probe signals at  $2023.5\text{ cm}^{-1}$  acquired in the “tilted” geometry as shown in the inset. The polarizations involved to record the parallel signal  $R_{||}^{\chi=60^\circ}$  are still all  $s$ -polarized. When the perpendicular signal  $R_{\perp}^{\chi=60^\circ}$  is recorded, however, the probe polarization is  $p$ -polarized. (C) To account for the difference in the geometry factors between the two data sets in the “normal” and the “tilted” geometries,  $R_{||}^{\chi=60^\circ}$  was matched to  $R_{||}^{\chi=0^\circ}$  by multiplying a scaling factor  $F$ , and  $R_{\perp}^{\chi=60^\circ}$  was multiplied by the same factor  $F$ . The three signals,  $R_{||}^{\chi=0^\circ} = F \times R_{||}^{\chi=60^\circ}$ ,  $R_{\perp}^{\chi=0^\circ}$ , and  $F \times R_{\perp}^{\chi=60^\circ}$ , are now absolutely comparable in amplitude to extract the orientational correlation functions and the population decay.

The data shown in Figure 3A and Figure 3B arise from the combinations of in-plane motions, out-of-plane motions, and vibrational relaxation processes. To quantitatively characterize the orientational dynamics at the surface, these contributions need to be separated. It has been shown in a previous publication how the observed signals are related to these three factors,<sup>14</sup> although this theoretical account did not include the local field correction. The local field correction was incorporated as discussed in the Supporting Information. The observed signals are written as

$$R_{||}^{\chi=0^\circ}(t) = A \times \left[ \frac{1}{9} - \frac{2}{9}\langle S \rangle + \frac{1}{9}C^{\text{op}}(t) + \frac{1}{8}C^{\text{mip}}(t) \right] \times P(t) \quad (3.1)$$

$$R_{\perp}^{\chi=0^\circ}(t) = A \times \left[ \frac{1}{9} - \frac{2}{9}\langle S \rangle + \frac{1}{9}C^{\text{op}}(t) - \frac{1}{8}C^{\text{mip}}(t) \right] \times P(t) \quad (3.2)$$

$$R_{||}^{\chi=60^\circ}(t) = B \times \left[ \frac{1}{9} - \frac{2}{9}\langle S \rangle + \frac{1}{9}C^{\text{op}}(t) + \frac{1}{8}C^{\text{mip}}(t) \right] \times P(t) \quad (3.3)$$

$$R_{\perp}^{\chi=60^\circ}(t) = B \times a_{p/s} \left[ \frac{1}{9} - \frac{1}{9}(3\cos^2\chi' - 1)\langle S \rangle + \frac{1}{9}(3\cos^2\chi' - 2)C^{\text{op}}(t) - \frac{1}{8}(\cos^2\chi')C^{\text{mip}}(t) \right] \times P(t) \quad (3.4)$$

where  $C^{\text{op}}(t)$  and  $C^{\text{mip}}(t)$  are orientational correlation functions corresponding to out-of-plane and mainly-in-plane motions given by

$$C^{\text{op}}(t) = \left\langle \frac{3\cos^2\theta(t) - 1}{2} \times \frac{3\cos^2\theta(0) - 1}{2} \right\rangle \quad (4.1)$$

$$C^{\text{mip}}(t) = \langle (e^{2i\phi(t)} \sin^2\theta(t))^* \times (e^{2i\phi(0)} \sin^2\theta(0)) \rangle \quad (4.2)$$

and  $P(t)$  is the population decay caused by vibrational relaxation.  $\langle \dots \rangle$  represents an ensemble average. These three time-dependent variables,  $C^{\text{op}}(t)$ ,  $C^{\text{mip}}(t)$ , and  $P(t)$ , are the three observables that will be obtained from the data. The  $p/s$  enhancement factor  $a_{p/s}$  and the effective incident angle  $\chi'$  are identical to the ones used in the IRLD experiment, and again for  $\chi = 60^\circ$ ,  $a_{p/s} = 1.011$  and  $\chi' = 49.72^\circ$ . The signals also depend on the order parameter  $\langle S \rangle$ , which we determined to be  $\langle S \rangle = -0.290 \pm 0.016$  by the time-averaged IRLD experiment. A and B are geometry factors depending on the geometry of the experiment, including the number of molecules in the focus and the pump/probe pulse local field amplitudes. By expanding eqs 3.1–3.4, it is clear that these are simultaneous linear equations with three unknown variables,  $A \times P(t)$ ,  $A \times P(t) \times C^{\text{op}}(t)$ , and  $A \times P(t) \times C^{\text{mip}}(t)$ , and one unknown factor  $F \equiv A/B$ .

Because  $R_{||}^{\chi=0^\circ}(t)$  and  $R_{\perp}^{\chi=0^\circ}(t)$  are measured with identical geometries (see Figure 3A inset) using the same laser pulses, these two signals have the identical geometry factor  $A$ .  $R_{||}^{\chi=60^\circ}(t)$  and  $R_{\perp}^{\chi=60^\circ}(t)$  have the same geometry factor  $B$  for the same reason, but  $A$  and  $B$  are different because the sample geometry is different, and the signals were obtained in independent experiments. This difference in the geometry factor can be accounted for by comparing  $R_{||}^{\chi=0^\circ}(t)$  and  $R_{||}^{\chi=60^\circ}(t)$ . In these two signals, the pump/probe polarizations are all  $s$ -polarized (in-plane) and parallel, so the time-dependences are identical. The only difference is in the geometry factors, as seen in eqs 3.1 and 3.3. Thus, the scaling factor  $F = A/B$  can be obtained by comparing the amplitudes of  $R_{||}^{\chi=0^\circ}(t)$  and  $R_{||}^{\chi=60^\circ}(t)$ .  $R_{||}^{\chi=60^\circ}(t)$  and  $R_{\perp}^{\chi=60^\circ}(t)$  are multiplied by the scaling factor  $F$  such that all the four signals have the identical geometry factor  $A$ . Figure 3C shows the four signals with the scaled  $R_{||}^{\chi=60^\circ}(t)$  and  $R_{\perp}^{\chi=60^\circ}(t)$ . As expected,  $R_{||}^{\chi=0^\circ}(t)$  and  $F \times R_{||}^{\chi=60^\circ}(t)$  are identical.

Now that the geometry factors in these signals are accounted for, the three signals  $R_{||}^{\chi=0^\circ}(t) = F \times R_{||}^{\chi=60^\circ}(t)$ ,  $R_{\perp}^{\chi=0^\circ}(t)$ , and  $F \times R_{\perp}^{\chi=60^\circ}(t)$  can be used to extract three unknown variables,  $A \times P(t)$ ,  $A \times P(t) \times C^{\text{op}}(t)$ , and  $A \times P(t) \times C^{\text{mip}}(t)$ , by solving the simultaneous linear equations.  $C^{\text{op}}(t)$  and  $C^{\text{mip}}(t)$  can then be obtained by dividing the last two by the first one. Because for  $P(t)$  we are only interested in the time-dependence, the factor  $A$  does not have to be eliminated, while  $C^{\text{op}}(t)$  and  $C^{\text{mip}}(t)$  have the

absolutely correct amplitude directly comparable with eqs 4.1 and 4.2. The extracted  $P(t)$ ,  $C^{\text{op}}(t)$ , and  $C^{\text{mip}}(t)$  are displayed in Figure 4, Figure 5A, Figure 6A, respectively.

It is important to recognize that the anisotropy  $(R_{\parallel} - R_{\perp})/(R_{\parallel} + 2R_{\perp})$  used to extract orientational correlation functions in three-dimensionally isotropic samples is not applicable here because the sample is not isotropic by the very existence of the planar surface. As given in eqs 3.1–3.4, the observed signals contain four physically relevant variables,  $\langle S \rangle$ ,  $P(t)$ ,  $C^{\text{op}}(t)$ , and  $C^{\text{mip}}(t)$ . To determine all four, one time-averaged measurement (time-averaged linear dichroism) and four time-dependent measurements,  $(R_{\parallel}^{\chi=0^{\circ}}(t), R_{\perp}^{\chi=0^{\circ}}(t), R_{\parallel}^{\chi=60^{\circ}}(t), \text{ and } R_{\perp}^{\chi=60^{\circ}}(t))$ , were employed with the measurement of  $R_{\parallel}^{\chi=60^{\circ}}(t)$  necessary for the scaling purpose.

When the measurement in the tilted geometry is conducted (Figure 3B), the tilt angle  $\chi$  should be set as large as possible because the larger tilt angle makes the difference between  $R_{\perp}^{\chi=0^{\circ}}(t)$  and scaled  $R_{\perp}^{\chi}(t)$  larger, which leads to more accuracy in the extracted  $C^{\text{op}}(t)$ .  $\chi = 60^{\circ}$  was used because that was the maximum possible tilt angle in the experimental setup. When another tilt angle  $\chi$  is used instead of  $\chi = 60^{\circ}$ , the identical  $C^{\text{op}}(t)$  and  $C^{\text{mip}}(t)$  should be obtained. As demonstrated in the Supporting Information (Figures S5 and S6),  $C^{\text{op}}(t)$  and  $C^{\text{mip}}(t)$  obtained with the tilt angle  $\chi = 45^{\circ}$  measurement agreed remarkably well with  $C^{\text{op}}(t)$  and  $C^{\text{mip}}(t)$  in Figure 5A and Figure 6A extracted with the  $\chi = 60^{\circ}$  measurement, demonstrating that the theory and the local field correction are accurate.

As seen in eq 4.2,  $C^{\text{mip}}(t)$  depends both on the polar and azimuthal angles, indicating that it is sensitive both to out-of-plane and in-plane motions of the molecules. Nonetheless, we refer to  $C^{\text{mip}}(t)$  as “mainly-in-plane” correlation function here because the out-of-plane motions for molecules bound at interfaces are often highly restricted, and the decay in  $C^{\text{mip}}(t)$  is likely to be dominated by in-plane motions of the molecules. We will show in the later sections that this is indeed the case for the monolayer sample studied here. Depending on the nature of samples, it is possible that there are significant out-of-plane motions as well; it is important to note, in that case, that  $C^{\text{mip}}(t)$  could be strongly affected by out-of-plane motions and should be referred to by another name. Even for such a sample with significant out-of-plane motions, however, the strategies discussed below to extract the dynamical nature of molecules based on  $C^{\text{op}}(t)$  and  $C^{\text{mip}}(t)$  are completely applicable.

**2.5. Population Decay  $P(t)$ .** The measured data are now decomposed into the three observables of interest, and each can be investigated in depth. The population decay,  $P(t)$ , is shown in Figure 4 (points). The population decay is proportional to the number of molecules in the excited state and does not contain contributions from orientational relaxation.  $P(t)$  was fit with a biexponential function with time constants of 2.1 and 21.4 ps (solid curve). The rhenium headgroup in a bulk solution exhibits a biexponential population decay as well. The rhenium headgroup has three CO stretch modes: one symmetric stretching mode ( $s$ ) at  $\sim 2023 \text{ cm}^{-1}$  and two antisymmetric stretching modes ( $as$ ) at  $\sim 1900 \text{ cm}^{-1}$ . Because we pumped only the  $s$  mode, the excited population in the  $s$  mode will quickly decay into  $as$  modes; relaxation and thermal excitation bring the three modes into thermal equilibrium. The fast 2.1 ps decay arises from this equilibration process. The slower 21.4 ps decay corresponds to the relaxation of the vibrational energy out of the CO stretching modes into other modes in the system such as vibrational modes of the phenanthroline ring, triazole ring and

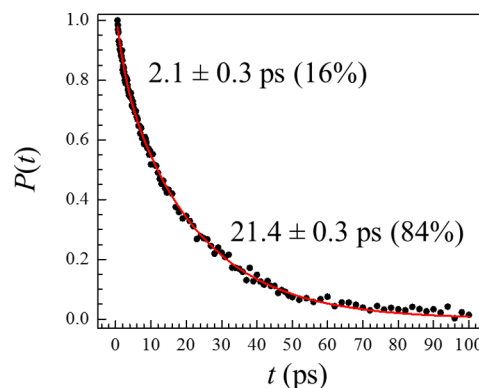


**Figure 4.** Population decay  $P(t)$  extracted from the PSAR–PP signals. The decay is biexponential with the time constants of 2.1 and 21.4 ps. The fast component is equilibration among the three CO stretching modes, and the slow component is vibrational relaxation to the ground state.

$C_{11}$  alkyl chains, and phonon modes of the silica substrate. Because the equilibration time among the CO stretch modes is fast compared to the vibrational relaxation, the 21.4 ps decay is the weighted average of the relaxation times of the individual CO stretch modes.

**2.6. Out-of-plane Correlation Function  $C^{\text{op}}(t)$ .** Our main interest is on the two orientational correlation functions, which are extracted without assuming a particular dynamical mechanisms. Of the two extracted orientational correlation functions,  $C^{\text{op}}(t)$  and  $C^{\text{mip}}(t)$ , we first discuss  $C^{\text{op}}(t)$  because it contains purely out-of-plane motions ( $\theta$ ) as in eq 4.1. The experimental  $C^{\text{op}}(t)$  is shown in Figure 5A (black points). For clarity, the data in Figure 5A were smoothed with five-point adjacent-averaging. Fits to smoothed and unsmoothed data gave the same results. The original data are the blue curve in Figure S6a.  $C^{\text{op}}(t)$  at very early time decays by a small amount and then reaches an offset level of  $\sim 0.23$ . Such a small decay followed by a very large offset shows that the out-of-plane motions are highly restricted. The offset value above zero was expected because the monolayer has ordering as indicated by time-averaged linear dichroism, and thus the headgroup cannot sample the full range of polar angle from  $0$ – $90^{\circ}$ .

Then the question is to what level would the correlation function be expected to decay? This question can be addressed by the order parameter  $\langle S \rangle \equiv \langle (3 \cos^2 \theta - 1)/2 \rangle$  measured by the IR linear dichroism. After infinitely long time where all the molecules sample all the possible configurations, the out-of-plane correlation function  $C^{\text{op}}(t)$  should reach the square of the order parameter  $\langle S \rangle^2$ :

$$\begin{aligned} C^{\text{op}}(\infty) &= \left\langle \frac{3 \cos^2 \theta(\infty) - 1}{2} \times \frac{3 \cos^2 \theta(0) - 1}{2} \right\rangle \\ &= \left\langle \frac{3 \cos^2 \theta(\infty) - 1}{2} \right\rangle \left\langle \frac{3 \cos^2 \theta(0) - 1}{2} \right\rangle \\ &= \left\langle \frac{3 \cos^2 \theta - 1}{2} \right\rangle^2 = \langle S \rangle^2 \end{aligned} \quad (5)$$

From the measured order parameter  $\langle S \rangle = -0.290$ ,  $\langle S \rangle^2$  was found to be 0.0841, which is plotted as a blue dashed line in Figure 5A. Clearly the offset level in the measured  $C^{\text{op}}(t)$  is significantly higher than  $\langle S \rangle^2$ , which indicates that not all of the out-of-plane angles are sampled in the time window of the

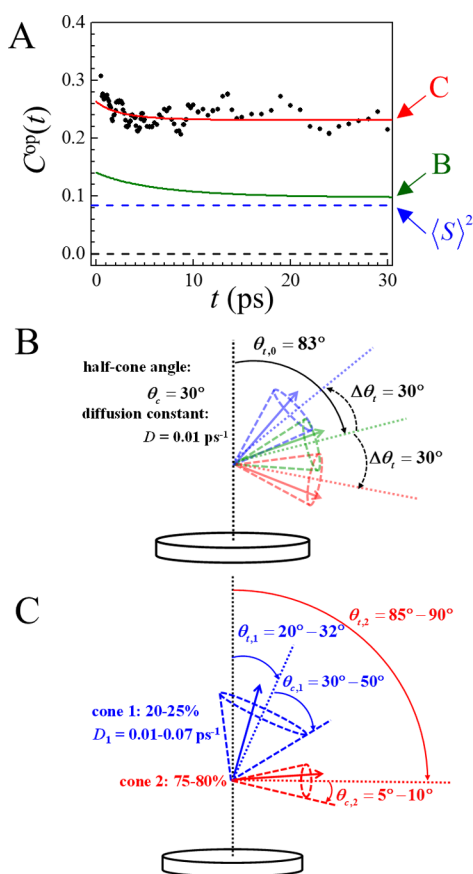


**Figure 5.** (A) Black points are the experimental out-of-plane correlation function  $C^{\text{op}}(t)$  extracted from the PSAR–PP signals. Blue dotted line:  $\langle S \rangle^2 = 0.084$  calculated based on the measured order parameter  $\langle S \rangle = -0.290$ . Green solid line: the fit to the observed  $C^{\text{op}}(t)$  using the “wobbling-in-a-range-of-tilted-cones” model shown in panel B. This model does not capture the large value of  $C^{\text{op}}(t)$ . Red solid line: the fit to  $C^{\text{op}}(t)$  using the “wobbling-in-two-cones” model shown in panel C, which reproduces the observed  $C^{\text{op}}(t)$ . (B) “Wobbling-in-a-range-of-tilted-cones” model, which provides the out-of-plane correlation function  $C^{\text{op}}(t)$  as the green solid line in panel A. While this model yields the order parameter of  $-0.291$ , which is consistent with the measured order parameter,  $C^{\text{op}}(t)$  was not reproduced. (C) “Wobbling-in-two-cones” model, which reproduced the observed  $C^{\text{op}}(t)$  well. The red line in panel A was generated with 22% of the molecules in cone 1 ( $\theta_{t,1} = 27^\circ$ ,  $\theta_{c,1} = 43^\circ$ ,  $D_1 = 0.05 \text{ ps}^{-1}$ ) and 78% of the molecules in cone 2 ( $\theta_{t,2} = 90^\circ$ ,  $\theta_{c,2} = 7.5^\circ$ ), which yields the order parameter  $\langle S \rangle = -0.287$  agreeing with the measured order parameter within the error. The calculated  $C^{\text{op}}(t)$  was not sensitive enough to  $D_2$  to uniquely determine its value.

experiments. Therefore, there are out-of-plane dynamics much slower than sub-ns or possibly static inhomogeneity in the polar angle distribution.

Now we can speculate what kind of angular motions and distributions of the molecules can reproduce the experimental  $C^{\text{op}}(t)$  decay and the order parameter  $\langle S \rangle$ . The wobbling-in-a-cone model has been commonly used and extremely successful for describing restricted motions of molecules in isotopic media.<sup>24–26</sup> To quantitatively characterize restricted molecular motions on surfaces, we have extended this model and developed “wobbling-in-a-tilted-cone” model.<sup>14</sup> As the name suggests, in this model we assume a transition dipole of interest is wobbling in a cone with a hard wall, which has a half-cone angle  $\theta_c$  and a

“tilt” angle  $\theta_t$ . The tilt angle is the angle between the surface normal and the cone axis.

The direct application of this model will not reproduce the measured  $C^{\text{op}}(t)$  and  $\langle S \rangle$  simultaneously because this model assumes that all the out-of-plane polar angles  $\theta$  within the cone are sampled by the wobbling motion, which is not the case here as discussed above. Thus, we first attempted to reproduce  $C^{\text{op}}(t)$  and  $\langle S \rangle$  by assuming that the transition dipoles are wobbling in ensembles of cones, the tilt angles of which continuously range from  $\theta_{t,0} - \Delta\theta_t$  to  $\theta_{t,0} + \Delta\theta_t$  with the identical cone angle  $\theta_c$  and the identical diffusion constant  $D$ , and each ensemble of cones does not exchange with each other on the time scale of the experiments (Figure 5B). We refer to this model as “wobbling-in-a-range-of-tilted-cones”. The functional forms of the out-of-plane correlation function and the order parameter for this model,  $C_{\text{range}}^{\text{op}}(t)$  and  $\langle S \rangle_{\text{range}}$  are given in the Supporting Information (eq S.29).  $\theta_{t,0}$ ,  $\theta_c$ ,  $\Delta\theta_t$ , and the diffusion constant  $D$  were varied so that the measured order parameter  $\langle S \rangle_{\text{range}}$  is maintained at  $-0.290 \pm 0.016$ , and the calculated  $C_{\text{range}}^{\text{op}}(t)$  is as close as possible to the measured  $C^{\text{op}}(t)$ . We found, however, that there is no combination of the parameters that simultaneously reproduces the low value of the measured order parameter  $\langle S \rangle = -0.290 \pm 0.016$  and the high value of the observed  $C^{\text{op}}(t) \approx 0.23$ . As an example, the green solid line in Figure 5A is the  $C_{\text{range}}^{\text{op}}(t)$  calculated with the cone parameters in Figure 5B. While this model yields the order parameter  $\langle S \rangle_{\text{range}} = -0.291$ ,  $C_{\text{range}}^{\text{op}}(t)$  is clearly missing the data. Apparently this model does not represent the distribution of molecules.

There is an interesting insight from the molecular dynamics (MD) simulation for an alkylthiol monolayer on a gold substrate with the identical terminal rhenium carbonyl headgroup and the identical chain length ( $C_{11}$ ) studied here.<sup>18</sup> This MD simulation not only reproduced the results of two-dimensional IR spectroscopy remarkably well, but also it predicted that the distribution of the polar angle  $\theta$  of the symmetric stretch mode’s transition dipole is bimodal, that is, peaked at two distinct angles. On the basis of these MD results, it is possible that the headgroup orientation distribution on the alkylsilane monolayer is bimodal as well.

Motivated by this prediction by MD simulation, we then attempted to fit  $C^{\text{op}}(t)$  and  $\langle S \rangle$  by assuming now that there are two distinct cones with different tilt angles and cone angles, and the exchange between these two cones does not happen on the experimental time scale (Figure 5C). Again, the analytical forms of the out-of-plane correlation function  $C_{\text{two cones}}^{\text{op}}(t)$  and the order parameter  $\langle S \rangle_{\text{two cones}}$  for this “wobbling-in-two-tilted-cones” model can be found in the Supporting Information (eq S.30). As shown as a red solid line in Figure 5A, this model indeed can reproduce the measured  $C^{\text{op}}(t)$  and the order parameter  $\langle S \rangle$  simultaneously. Thus, our measured set of  $C^{\text{op}}(t)$  and  $\langle S \rangle$  indicates that the orientational distribution is likely to be bimodal as in Figure 5C, rather than a continuous distribution as in Figure 5B. The order parameter  $\langle S \rangle$  obtained in time-averaged linear dichroism measurement only provides the average angle, not the distribution. It is remarkable that the extracted  $C^{\text{op}}(t)$  not only contains the information about the dynamics, but also can distinguish among models of the polar angular distribution of the molecules at the surface.

As shown in Figure 5C, one of the cones (cone 1) is tilted at  $20^\circ$ – $32^\circ$  with the cone half angle of  $30^\circ$ – $50^\circ$ . The diffusion constant was estimated to be  $0.01$ – $0.07 \text{ ps}^{-1}$ , which is the main source of the early decay in  $C^{\text{op}}(t)$ . Because the transition dipoles in this cone have a relatively high degree of dynamical freedom,

these molecules might reside in isolated sites. Another cone (cone 2) is almost lying in the plane of the surface with the 85–90° transition dipole tilt angle. As the very small cone angle of 5–10° indicates, the motions are more restricted than those of cone 1. The majority of the molecules are wobbling in the cone 2 (75–80%), while molecules in the cone 1 are a minor component (20–25%). The wobbling in cone 2 does not cause a significant decay of  $C^{\text{op}}(t)$ , and thus we were unable to determine the diffusion constant for this second cone. At long time, >sub-ns, these two types of configurations may switch with each other, which will complete the out-of-plane motion of the transition dipoles and yield  $C^{\text{op}}(\infty) = \langle S \rangle^2$ . The existence of such slow out-of-plane motions of interfacial molecules has been suggested by polarization-selective time-resolved SHG experiments.<sup>9</sup>

**2.7. Mainly-in-plane Correlation Function  $C^{\text{mip}}(t)$ .** Figure 6A shows the mainly-in-plane correlation function (black points) in eq 4.2 obtained from the experimental measurements, which contains both in-plane ( $\phi$ ) and out-of-plane ( $\theta$ ) angular motion. It can be seen that in contrast to  $C^{\text{op}}(t)$ ,  $C^{\text{mip}}(t)$  is decaying to zero. Because the monolayer should be macroscopically isotropic in the plane of the surface,  $C^{\text{mip}}(t)$  should indeed decay to zero at sufficiently long time.

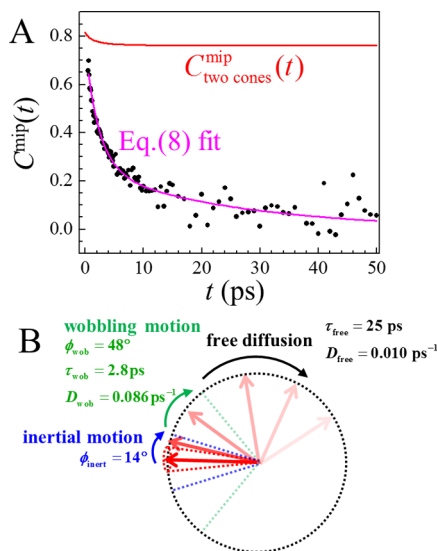


**Figure 6.** (A) Black: the experimental mainly-in-plane correlation function  $C^{\text{mip}}(t)$  extracted from the PSAR–PP signals. Red:  $C^{\text{mip}}_{\text{two cones}}(t)$  calculated with “wobbling-in-two-cones” model using the parameters given in the Figure 5C caption. Again,  $C^{\text{mip}}_{\text{two cones}}(t)$  was insensitive to the value of  $D_2$ . Magenta: the fit to the experimental  $C^{\text{mip}}(t)$  with eq 8. (B) The in-plane dynamics of the molecules extracted from  $C^{\text{mip}}(t)$ . The in-plane distribution of molecules immediately diffuse over the inertial sector (blue), then further diffuse in the wobbling sector (green), and then are completely randomized by the free diffusion process.

Again, the extraction of  $C^{\text{mip}}(t)$  does not depend on assumptions of the depolarization mechanism. It is in principle possible that the depolarization is caused by Förster excitation transfer arising from the dipole–dipole interaction between the head groups rather than the orientational motions of our interest.<sup>27</sup> In the Supporting Information, we show that the contribution from Förster excitation transfer to  $C^{\text{mip}}(t)$  cannot be a significant depolarization mechanism here based on the previous two-dimensional IR spectroscopy measurements,<sup>16</sup> the temporal profile, and the head groups’ loading dependence of the 2D anisotropy decay (Figure S9). In the following

discussion, we will attribute the decay in  $C^{\text{mip}}(t)$  to the reorientation of the transition dipoles.

We showed from the measured  $C^{\text{op}}(t)$  that the out-of-plane molecular motions are well represented by wobbling-in-two-tilted-cones model shown in Figure 5C. We can calculate how the motion in Figure 5C contributes to  $C^{\text{mip}}(t)$  decay. The calculated  $C^{\text{mip}}(t)$  decay based on the motions in Figure 5C,  $C^{\text{mip}}_{\text{two cones}}(t)$ , is plotted as a red solid line in Figure 6A. The observed  $C^{\text{mip}}(t)$  decays much faster and to a much greater extent than  $C^{\text{mip}}_{\text{two cones}}(t)$ , demonstrating that the out-of-plane motions are not a major contribution to the  $C^{\text{mip}}(t)$ , and the  $C^{\text{mip}}(t)$  is dominated by purely in-plane motions, that is, the decay in  $\langle (e^{2i\phi(t)}) * e^{2i\phi(0)} \rangle$ . Thus, for the sample studied here, the decay in the mainly-in-plane correlation function  $C^{\text{mip}}(t)$  arises from in-plane motions, as its name suggests.

The decay of  $C^{\text{ip}}(t) = \langle (e^{2i\phi(t)}) * e^{2i\phi(0)} \rangle$  can be caused by unrestricted diffusive motions or a combination of restricted and unrestricted motions of the transition dipoles in the plane of the surface. Purely unrestricted free diffusion would give a single exponential decay. However, fitting the observed data in Figure 6A yields a biexponential with time constants of 2.35 and 24.5 ps. These results show that a single unrestricted diffusive process does not account for the data.

We can model the restricted in-plane reorientation by a two-dimensional version of the wobbling-in-a-cone model, which we refer to as “wobbling-in-a-sector” model. In this model, a transition dipole is wobbling in the plane of the surface with a diffusion constant  $D$  in a limited range of azimuthal angle  $2\phi_c$ , where  $2\phi_c$  is a full sector angle, without changing the polar angle  $\theta$ .  $C^{\text{ip}}(t) = \langle (e^{2i\phi(t)}) * e^{2i\phi(0)} \rangle$  can be calculated based on this model and yields

$$C^{\text{ip}}(t) = [\text{sinc}(2\phi_w)]^2 + (1 - [\text{sinc}(2\phi_w)]^2) \exp[-t/\tau_w] \quad (6)$$

where  $w$  stands for wobble. The derivation (eqs S.31–S.42) and the dependence of  $\tau_w$  on the sector angle and the diffusion constant for the restricted motion are given in the Supporting Information. The in-plane anisotropy decay for the unrestricted rotational diffusion case was shown by Bonn and co-workers to be<sup>28</sup>

$$C^{\text{ip}}(t) = \exp[-4D_{\text{free}}t] \quad (7)$$

As Tan et al. showed,<sup>29</sup> when there are several independent motions contributing to the decay of orientational correlation function, the effect of additional motions can be incorporated by multiplying the normalized orientational correlation functions corresponding to the additional motions. Noting that the in-plane correlation functions in eqs 6 and 7 are normalized to 1, these correlation functions can be directly multiplied to yield the mainly-in-plane function. The successful fit was obtained when the  $C^{\text{mip}}(t)$  was constructed in the form of

$$C^{\text{mip}}(t) = C^{\text{mip}}_{\text{two cones}}(t) \times C^{\text{ip,sec}}_{\text{inert}}(t) \times C^{\text{ip,sec}}_{\text{wob}}(t) \times C^{\text{ip,free}}(t) \quad (8)$$

This function accounts for the contribution from the out-of-plane motions, the initial ultrafast inertial decay, the in-plane wobbling motion, and the final complete diffusive randomization.  $C^{\text{mip}}_{\text{two cones}}(t)$  is an unnormalized mainly-in-plane correlation function arising from two-cones motion in Figure 5C.  $C^{\text{ip,sec}}_{\text{inert}}(t) = [\text{sinc}(2\phi_{\text{c,inert}})]^2$  (obtained as  $\tau_{\text{corr}} \rightarrow 0$  in eq S.41) is the in-plane inertial correlation function necessary to account for the amplitude difference between the observed  $C^{\text{mip}}(t)$  and

$C_{\text{two cones}}^{\text{mip}}(t)$  at  $t = 0$ .  $C_{\text{wob}}^{\text{ip,sec}}(t) = [\text{sinc}(2\phi_w)]^2 + (1 - [\text{sinc}(2\phi_w)]^2) \exp(-t/\tau_w)$  (eq 6) accounts for the fast decay in the observed mainly-in-plane correlation function arising from an in-plane wobbling motion, and  $C^{\text{ip,free}}(t) = \exp(-4D_{\text{free}}t)$  (eq 7) accounts for the fast slow decay of the observed mainly-in-plane correlation function.

Figure 6B summarizes the in-plane motion of the transition dipoles extracted from the observed  $C^{\text{mip}}(t)$  through the fit with eq 8. While the transition dipoles are distributed in the two cones in Figure 5C, the transition dipoles in cone 2 are the dominant contribution to the mainly-in-plane correlation function  $C^{\text{mip}}(t) = \langle (e^{2i\phi(t)} \sin^2 \theta(t))^* \times (e^{2i\phi(0)} \sin^2 \theta(0)) \rangle$  because  $\sin^4 \theta_{t,2} \gg \sin^4 \theta_{t,1}$  and also the population in cone 2 is larger than those in cone 1 roughly by a factor of 4. Thus, the motions illustrated schematically in Figure 6B can be regarded as the in-plane motions of the transition dipoles in cone 2 in Figure 5C.

While the polar (out-of-plane) angles of the transition dipoles are strongly restricted with very little reorientation on in the time window of the experiments, there are substantial in-plane dynamics. As Figure 6B suggests, a transition dipole pointing toward one direction at a certain time point immediately spreads out over a sector with half-sector angle of  $14^\circ$ . Over the next 2.8 ps, the transition dipole diffuses over a larger sector of the half-sector angle  $48^\circ$  with the diffusion constant of  $0.086 \text{ ps}^{-1}$ . Then the transition dipole undergoes free diffusion with the diffusion constant of  $0.010 \text{ ps}^{-1}$ , and by 50 ps, as shown in Figure 6A, the free diffusion is almost complete. The free diffusion orientation relaxation time constant is  $\sim 25$  ps.

The results show that the headgroup can reorient rapidly in the plane of the surface. This fast reorientational dynamics of the headgroup of a functionalized alkyl chain monolayer is foreshadowed by previous reports that studied reorientation of interfacial molecules on slower time scales. For example, Watarai and co-workers studied nanosecond in-plane motions of a relatively large fluorophore at the toluene–water interface by fluorescence depolarization measurements.<sup>8</sup> They showed that on top of the nanosecond motion, which they were able to characterize in detail, there also existed significant faster motions, which could not be captured with their sub-ns time resolution. Blanchard and co-workers studied a pyrene-terminated monolayer on an  $\text{SiO}_2$  surface and essentially probed the in-plane fluorescence depolarization<sup>30</sup> and found that for some of their monolayers the anisotropy was very low, even at the minimum delay time they were able to measure with their time resolution. Thus, very fast in-plane motions of interfacial molecules have been suggested by these results. The IR PSAR–PP experiments make it possible to probe fast orientational relaxation and obtain information on both the in-plane and out-of-plane dynamics with picosecond time resolution.

Considering that the metal carbonyl headgroup structure itself is rigid, the observed in-plane motions are associated with physical motions of the alkyl chains. MD simulations on  $\text{C}_{11}$ – $\text{RePhen}(\text{CO})_3\text{Cl}$  thiol monolayers on gold substrates can provide insights into the nature of the motions.<sup>18</sup> The MD simulations showed that the spectral diffusion in the thiol monolayers observed by two-dimensional IR spectroscopy is induced by dihedral flips between gauche and anticonformers, that is, rotations around C–C bonds in the alkyl chains, and also triazole ring rotations. The dihedral flip rate and the triazole ring rearrangement rate depended on the percentage of the gauche defects in the alkyl chains and were accelerated as the gauche defects in the alkyl chains were increased. In the simulations, for the monolayer with 6% of gauche defects, which is a relatively

small percentage, the dihedral flip and the triazole ring rearrangement occurred on time scales of approximately 25 and 90 ps, respectively. When the gauche defect number was increased to 15%, the dihedral flip and the triazole ring rearrangement became more frequent and were observed on time scale of approximately 20 and 70 ps, respectively. The alkylsiloxane monolayer studied here is known to contain more gauche defects than the well-packed and highly ordered thiol monolayers,<sup>16</sup> and therefore the dihedral flip and the triazole ring rearrangement may be even more frequent. Because these motions induce changes in the in-plane orientations of the headgroups, it is likely that the appearance and disappearance of gauche defects and the triazole ring rearrangements are the dominant sources of the observed in-plane reorientation.

### 3. CONCLUDING REMARKS

We have demonstrated the application of IR polarization-selective angle-resolved pump–probe spectroscopy to the measurement of orientational dynamics of a monolayer functionalized with a metal carbonyl headgroup. By resolving the incident angle as well as the input polarizations, the in-plane and out-of-plane picosecond motions of the headgroup were independently extracted. The out-of-plane and in-plane motions were characterized as in Figure 5C and Figure 6B. Information on the out-of-plane angular distribution of the head groups was obtained through physical models of the out-of-plane correlation function. A single continuous range of the polar angle distribution was not able to reproduce the observed out-of-plane correlation function and the order parameter simultaneously; therefore, the distribution of the molecules is multimodal. A bimodal distribution, which is the simplest multimodal distribution and is also supported by a previous MD simulation, reproduced all the experimental observables.

PSAR–PP spectroscopy is applicable as long as the molecules of interest are located only at an interface and a sample substrate transmits the probe beam. Thus, PSAR–PP can be extended to study other types of monolayers, such as Langmuir films at liquid–air interfaces. The molecules of interest are required to interact with IR beams strongly to obtain sufficient signal, but note that in this study we reduced the pump intensity by a factor of  $\sim 6$  to avoid the saturation of the transition. For the molecules with smaller transition dipoles, the transition can be pumped harder. Therefore, it is likely to be possible to apply PSAR–PP spectroscopy to interfacial molecules with much smaller size and transition dipole than the metal carbonyl studied here. The technique is not applicable for the molecules on a completely reflective surface because all the polarizations become parallel to the surface normal right at the surface, and the polarization dependence cannot be studied.<sup>18</sup>

Picosecond motions of the type of sample studied here could be studied by polarization-selective time-resolved SFG (TRSFG) spectroscopy. However, while PSAR–PP spectroscopy is a third-order spectroscopy with three dipole interactions, TRSFG is a fourth-order spectroscopy, which involves three dipole interactions and one polarizability interaction. Therefore, the functional forms of the response functions for TRSFG are inherently more complicated than eqs 3.1–3.4 for PSAR–PP and also depend on the form of the polarizability tensor.<sup>31</sup> Because of the complexity of the response functions, so far no equivalent TRSFG method has been developed to extract in-plane and out-of-plane orientational correlation functions in a model-independent manner, and the observed signals have been interpreted assuming that molecules obey a predetermined

dynamical model. Thus, PSAR–PP has an advantage over TRSFG in terms of simplicity and interpretability. TRSFG is advantageous when the interfacial molecules of interest are the same molecules that make up the bulk liquid, such as dangling hydroxyl groups at the water–air interface as studied by Bonn and co-workers.<sup>10</sup> While TRSFG is interface-selective, PSAR–PP signals are overwhelmed by signals from a bulk solvent. Therefore, these two methods are complementary, and one of the techniques should be chosen depending on the nature of sample.

Note that in-plane and out-of-plane correlation functions extracted in Figures 5A and Figure 6A do not involve assumptions or models of the nature of molecular dynamics. For isotropic samples, it has been a recent trend to compare an experimentally observed orientational correlation function  $C_2(t) = 2.5 \times (R_{\parallel}(t) - R_{\perp}(t)) / (R_{\parallel}(t) + 2R_{\perp}(t))$  with a MD simulated orientational correlation function  $C_2(t) = \langle P_2(\hat{\mu}(t) \cdot \hat{\mu}(0)) \rangle$  to see if MD simulations are capturing the dynamics of the molecules properly.<sup>32</sup> The same strategy is now applicable for surface samples. The experimentally observed  $C^{\text{op}}(t)$  and  $C^{\text{mip}}(t)$  in Figures 5A and Figure 6A are directly comparable with the correlation functions calculated from eqs 4.1 and 4.2 using MD simulations. For the particular alkylsiloxane monolayer studied here, a MD simulation has not been performed.

The methodology demonstrated here to obtain model independent in-plane and out-of-plane orientational correlation functions can be directly extended to other third-order spectroscopic methods as well such as fluorescence depolarization. While fluorescence depolarization experiments to study interfacial molecules have been applied under the assumption that in-plane and out-of-plane motions are decoupled,<sup>6–8</sup> the model-independent  $C^{\text{op}}(t)$  and  $C^{\text{mip}}(t)$  extracted with the method presented here will allow more detailed and accurate characterization of surface molecular dynamics.

## ■ ASSOCIATED CONTENT

### Supporting Information

The Supporting Information is available free of charge on the ACS Publications website at DOI: 10.1021/jacs.6b08672.

Local field corrections for IRLD and PSAR–PP experiments, sample preparation, time-averaged IR linear dichroism details, PSAR–PP spectroscopy method, experimental details, orientational correlation functions for numerical models, Förster excitation transfer analysis (PDF)

## ■ AUTHOR INFORMATION

### Corresponding Author

\*fayer@stanford.edu

### Notes

The authors declare no competing financial interest.

## ■ ACKNOWLEDGMENTS

This material is based upon work supported by the Air Force Office of Scientific Research under AFOSR Award No. FA9550-16-1-0104. We thank Patrick Kramer for useful discussions. J.N. and C.Y. also thank the Stanford Graduate Fellowship program for graduate fellowships.

## ■ REFERENCES

(1) Terry, T. J.; Stack, T. D. P. *J. Am. Chem. Soc.* **2008**, *130*, 4945.

(2) Fraile, J. M.; García, J. I.; Herrerías, C. I.; Mayoral, J. A.; Pires, E. *Chem. Soc. Rev.* **2009**, *38*, 695.

(3) Shen, Y. *Annu. Rev. Phys. Chem.* **1989**, *40*, 327.

(4) Zhuang, X.; Miranda, P. B.; Kim, D.; Shen, Y. R. *Phys. Rev. B* **1999**, *59*, 12632.

(5) Yamaguchi, S.; Hosoi, H.; Yamashita, M.; Sen, P.; Tahara, T. *J. Phys. Chem. Lett.* **2010**, *1*, 2662.

(6) Wirth, M. J.; Burbage, J. D. *Anal. Chem.* **1991**, *63*, 1311.

(7) Wirth, M.; Burbage, J. *J. Phys. Chem.* **1992**, *96*, 9022.

(8) Tsukahara, S.; Yamada, Y.; Watarai, H. *Langmuir* **2000**, *16*, 6787.

(9) Zimdars, D.; Dadap, J.; Eienthal, K. B.; Heinz, T. *J. Phys. Chem. B* **1999**, *103*, 3425.

(10) Hsieh, C.-S.; Campen, R. K.; Vila Verde, A. C.; Bolhuis, P.; Nienhuys, H.-K.; Bonn, M. *Phys. Rev. Lett.* **2011**, *107*, 116102.

(11) Moilanen, D. E.; Fenn, E. E.; Lin, Y. S.; Skinner, J. L.; Bagchi, B.; Fayer, M. D. *Proc. Natl. Acad. Sci. U. S. A.* **2008**, *105*, 5295.

(12) Woutersen, S.; Bakker, H. J. *Nature* **1999**, *402*, 507.

(13) Woutersen, S.; Emmerichs, U.; Bakker, H. J. *Science* **1997**, *278*, 658.

(14) Nishida, J.; Fayer, M. D. *J. Chem. Phys.* **2014**, *140*, 144702.

(15) Rosenfeld, D. E.; Gengeliczki, Z.; Smith, B. J.; Stack, T. D. P.; Fayer, M. D. *Science* **2011**, *334*, 634.

(16) Rosenfeld, D. E.; Nishida, J.; Yan, C.; Gengeliczki, Z.; Smith, B. J.; Fayer, M. D. *J. Phys. Chem. C* **2012**, *116*, 23428.

(17) Yan, C.; Yuan, R.; Nishida, J.; Fayer, M. D. *J. Phys. Chem. C* **2015**, *119*, 16811.

(18) Yan, C.; Yuan, R.; Pfalzgraff, W. C.; Nishida, J.; Wang, L.; Markland, T. E.; Fayer, M. D. *Proc. Natl. Acad. Sci. U. S. A.* **2016**, *113*, 4929.

(19) Kramer, P. L.; Nishida, J.; Fayer, M. D. *J. Chem. Phys.* **2015**, *143*, 124505.

(20) Heinz, T. F. *Nonlinear Surface Electromagnetic Phenomena* **1991**, *29*, 353.

(21) Shim, S.-H.; Zanni, M. T. *Phys. Chem. Chem. Phys.* **2009**, *11*, 748.

(22) Nishida, J.; Tamimi, A.; Fei, H.; Pullen, S.; Ott, S.; Cohen, S. M.; Fayer, M. D. *Proc. Natl. Acad. Sci. U. S. A.* **2014**, *111*, 18442.

(23) Marroux, H. J.; Orr-Ewing, A. J. *J. Phys. Chem. B* **2016**, *120*, 4125.

(24) Kinoshita, K., Jr.; Kawato, S.; Ikegami, A. *Biophys. J.* **1977**, *20*, 289.

(25) Lipari, G.; Szabo, A. *Biophys. J.* **1980**, *30*, 489.

(26) Wang, C. C.; Pecora, R. J. *Chem. Phys.* **1980**, *72*, 5333.

(27) Baumann, J.; Fayer, M. D. *J. Chem. Phys.* **1986**, *85*, 4087.

(28) Nienhuys, H.-K.; Bonn, M. *J. Phys. Chem. B* **2009**, *113*, 7564.

(29) Tan, H.-S.; Piletic, I. R.; Fayer, M. J. *Chem. Phys.* **2005**, *122*, 174501.

(30) Dominska, M.; Kryszinski, P.; Blanchard, G. J. *J. Phys. Chem. B* **2005**, *109*, 15822.

(31) Gengeliczki, Z.; Rosenfeld, D. E.; Fayer, M. D. *J. Chem. Phys.* **2010**, *132*, 244703.

(32) Laage, D.; Thompson, W. H. *J. Chem. Phys.* **2012**, *136*, 044513.